

Heteroatoms Doped Hierarchical Porous Carbon Materials for High Performance Supercapacitor Electrodes

Haoan Que¹, Chengshuai Chang¹, Xuena Yang^{1,2,3}, Feng Jiang¹, Mei Li^{1,2,3,*}

¹ School of Materials Science and Engineering, Qilu University of Technology (Shandong Academy of Sciences), Jinan 250353, P.R. China.

² Shandong Provincial Key Laboratory of Processing and Testing Technology of Glass and Functional Ceramics, Jinan 250353, P.R. China.

³ Key Laboratory of Amorphous and Polycrystalline Materials, Qilu University of technology, Jinan 250353, P.R. China.

*E-mail: lim@qlu.edu.cn

Received: 7 December 2018 / Accepted: 10 January 2019 / Published: 10 March 2019

Hierarchical porous carbon materials (HPC) based on sulfur-urea-formaldehyde resins have been prepared with different size of silicas as templates, following by carbonization and alkaline etching. When tested in 6 M KOH, the storage capacitance of HPC is as high as 625 F g⁻¹ at 1.0 A g⁻¹, showing excellent rate capability (288 F g⁻¹ at 10 A g⁻¹). Furthermore, HPC possess remarkable electrochemical cycling stability (less than 4.0% loss after 5000 cycles) when tested at 10 A g⁻¹. At the same time, the energy density (*E*) of HPC was 12.5 and 44.6 Wh kg⁻¹ at the power density (*P*) of 288 and 300 W kg⁻¹ with the electrolytes of 6 M KOH and 1 M LiPF₆ in EC/DEC at the corresponding test systems illustrating this materials has potential practical application potential. The superior capacitive performances resulted from its high surface area, hierarchical micro/meso/macroporous structures and heteroatoms doping of the HPC, which providing the ideal storage capacity, fast transport speed of electrolyte ions, and outstanding synergistic effect of doped heteroatoms. These results demonstrate that the HPC electrode materials with unique pore structure and chemical composition hold particularly promising prospect as supercapacitors.

Keywords: hierarchical porous carbon materials; heteroatom doping; supercapacitors; specific capacitance; rate capacity

1. INTRODUCTION

In last few years, there are ever-increasing demands for green and environmentally benign energy due to the fast economic development and environmental degradation [1, 2]. Therefore, considerable efforts have been made to address the development of new-style energy conversion and storage devices.

Owing to their high power density, long cycling durability and fast charge/discharge capability, supercapacitors have attracted tremendous attention and been applied in various fields [3, 4].

It is well known that supercapacitors can be categorized into two categories: electrical double layer capacitors (EDLCs) such as carbon materials and pseudocapacitors just like transition metal oxides and conducting polymers [5-7]. During the development of EDLCs, control over both the specific area (S_{BET}) and pore structure of electrode materials plays a crucial role in ensuring good performance of the supercapacitor [8, 9]. It has been well demonstrated that heteroatoms doping can not only improve the storage capacity by introducing additional pseudocapacitance, but also enhance surface wettability of materials so the increase of surface area would be more efficient and consequently improve the whole electrochemical performance of the electrode materials [5, 9, 10].

Porous carbon materials have been demonstrated to possess many advantages and therefore arouse wide interests for advanced supercapacitors materials [11, 12]. Two most effective means have been focused on to meet demands mentioned above. One is optimizing the pore structure including the aperture size and distribution [13, 14], the other is introducing heteroatoms into the carbon network to bring pseudocapacitance from the extra faradic redox reactions [15, 16].

Recently, hierarchical porous carbon materials with combination of different size of pore diameter have attracted scientists' attention because of their various application in supercapacitors [17-19]. Micropores can significantly enhance the storage capacity because they greatly increase the specific surface area [20]. Mesopores play a significant role in providing channel for ion diffusion, so the electrochemical property can reach a high level, while macropores serve as a reservoir of ion and improve the efficiency of ion diffusion [21, 22]. Therefore, hierarchical porous carbon materials with optimum pore structure possess many unique advantages and a very bright prospect [23, 24].

Sorts of methods including activation process and template have been researched for preparation of hierarchical porous carbon materials to achieve better electrochemical performances for supercapacitors [25, 26]. Song et al. synthesized a kind of hierarchically ordered mesoporous carbon/graphene (OMC/G) nanocomposites by means of hydrothermal method [27]. Subsequently, when the resulted nanocomposites were used as supercapacitor electrode materials, it exhibit an excellent capacitance as high as 395.5 F g^{-1} at 0.5 A g^{-1} in 6 M KOH electrolyte, that is much higher than that of OMC (234.2 F g^{-1}) and OMC composites (217.7 F g^{-1}). Zhu et al. prepared a hierarchical porous carbons (HPCs) with high specific area $1371 \text{ m}^2 \text{ g}^{-1}$ [28].

Moreover, the structural design, introducing heteroatoms such as nitrogen (N), sulfur (S), oxygen (O), phosphorus (P) and boron (B) in the electrode carbon framework is an another important way improve the supercapacitor performance [29-31]. These heteroatoms can not only generate reversible pseudocapacitance effectively but also enhance electronic conductivity and wettability of the obtained materials. N-doped carbon materials have great promise in achieving high energy density supercapacitors in recent years [32, 33]. Wang et al. fabricated nitrogen-doped porous carbon (NPCs) by activation process, and as the supercapacitors electrode, the NPCs exhibited excellent electrochemical performance with a high specific capacitance of 343 F g^{-1} at current density 0.5 A g^{-1} in $1 \text{ M H}_2\text{SO}_4$ aqueous electrolyte and a wonderful rate capability of 234 F g^{-1} at current density 30 A g^{-1} [34]. Zhou et al. prepared a novel heteroatoms doped carbon electrode materials with high specific capacitance of 250 F g^{-1} in KOH electrolyte [35].

In this paper, 15 and 100 nm silicas were used as templates to prepare hierarchical porous carbon materials from sulfur-urea-formaldehyde resins via carbonization and alkaline etching. Systematic physicochemical analysis of the sample at each stage of preparation was carried out by a variety of tests, including SEM for surface morphology, XPS for surface elemental composition, FTIR for functional groups, TGA for thermal stability, and BET for surface area measurement. Crystallinity and phase information were revealed by XRD and TEM techniques. The specific electrochemical capacitance, retention rate, and charge-discharge cycling stability were evaluated by the standard electrochemical methods, such as cyclic voltammetry (CV), galvanostatic charge-discharge (GCD) and electrochemical impedance spectroscopy (EIS). And the energy density (E) and power density (P) of prepared materials were measured in different symmetrical electrodes systems.

2. EXPERIMENTAL

2.1. Chemicals

Thiourea (H_2NCSNH_2) and formaldehyde solution were purchased from Shandong Zhongke and Shenyang Laibo Chemical Co. Ltd, respectively. Hydrochloric acid (HCl), silicic acid tetrachlyl ester and ammonium hydroxide were purchased from Weihai Shengqi Chemical Reagent Factory. 15 nm silicon dioxide (SiO_2) was purchased from Aladdin. All reagents were in analytical grade and used without further purification.

2.2. Preparation of SiO_2 nanospheres

6.0 ml ammonium hydroxide was added into 100 ml ethanol solution, and 3 ml silicic acid tetrachlyl ester was dropwise added into the above solution then stirred at 25 °C for 12 h. The resultant white suspension was filtrated and washed six times by deionized water and ethanol. The final products were dried at 40 °C for 8 h.

2.3. Preparation of hierarchical carbon materials

First, 17.52 g H_2NCSNH_2 and 6.0 ml formaldehyde solution (37.0 %) were transferred into the 100.0 ml deionized water under mechanical stirring at 55 °C. During the process of stirring, 0.4 ml HCl was injected into the above mixed solution. It was further stirred and reacted for 3 h at 55 °C and an opalescent suspension liquid of resin matrix was obtained. After cooling naturally, the obtained matrix was filtrated, washed and then freeze-dried to obtain opalescent powder. Then the resin matrix was carbonized at 750 °C for 3 h in the tube furnace under Ar gas flow and finally microporous carbon materials were obtained and named as single pore size carbon (SPC).

Secondly, 1.0 g, 15 nm SiO_2 was dispersed into 100.0 ml deionized water, then 17.52 g H_2NCSNH_2 , 6 ml formaldehyde solution, and 0.4 ml HCl were added into above solution. After the same process of synthetic and carbonization, carbon materials containing the SiO_2 template were prepared. Then 0.5 g carbon materials were added into 0.2 M NaOH solution and etched for 10 h at 80 °C, finally the micro-mesoporous carbon materials were synthesized and named as double pore size carbon (DPC).

Lastly, 1.5 g, 15 nm SiO₂ and 2.0 g SiO₂ nanospheres were added into 100.0 ml deionized water and ultrasonic dispersed for 2 h, then 17.52 g H₂NCSNH₂, 6.0 ml formaldehyde solution and 0.4 ml HCl were injected into the above solution. After the same synthetic process, carbonization and etching, the micro-meso-macroporous carbon materials were obtained and named as hierarchical porous carbon (HPC).

2.4. Material characterization

Transmission electron microscopy (TEM, JEM-2100) and scanning electron microscopy (SEM, Hitachi S-4800) were performed at an accelerating voltage of 200 kV and 5 kV for the investigation of microstructure and morphology, respectively. Thermal gravimetric analysis (TGA) was proceeded on Perkin-Elmer, TG7, under N₂ flow. Energy-dispersive spectroscopy (EDS) mapping images were got from a Hitachi S-4800 field-emission scanning electron microscope. Fourier transformation infrared (FTIR) spectra were performed on a TENSOR 27 FTIR spectrometer. X-ray diffraction (XRD) patterns were obtained on a Bruker D8 ADVANCE (Cu K α , 1.54178 Å). Two-probe technique X-ray photoelectron spectroscopy (XPS) measurements were conducted on a Thermo Fisher Scientific ESCALAB 250 spectrometer. Raman spectra were performed using a Renishaw InVia microRaman system with a 514 nm Ar⁺ ion laser. The pore size distribution (PSD) plot was estimated by BJH (Barrett-Joyner-Halendar) method and S_{BET} was calculated by the conventional BET (Brunauer-Emmett-Teller) method.

2.5. Electrochemical measurements

Electrochemical properties of all the materials were performed on an electrochemical working station (CHI 660E, Chenhua Limited Co. Shanghai, China). In three-electrode system, Cyclic voltammetry (CV), galvanostatic charge-discharge (GCD) and electrochemical impedance spectroscopy (EIS) plots were achieved. And the saturated calomel electrode was used as the reference electrode, platinum sheet as the counter electrode and 6 M KOH solution as the electrolyte. The obtained materials, polytetrafluoroethylene (PTFE) and acetylene black with a mass ratio of 80:10:10 were mingled uniformly by adding a small amount of poly (vinylidene fluoride) (PVDF). And the above mixture was coated on a 1 cm×1 cm stainless steel wire mesh current collector, and dried at 60 °C for 8 h. The gravimetric capacitance (C_g , F g⁻¹) of the prepared materials was calculated from the GCD curve based on the following equation (1):

$$C_g = \frac{I \times \Delta t}{m \times \Delta V} \quad (1)$$

Where I (A) was the discharge current, Δt (s) was the discharge time, ΔV (V) was the potential window, and m (g) was the mass of active material on the working electrode.

In a two-electrode system, the supercapacitors were assembled in asymmetrical configuration and separated by a celgard 2400 membrane to form a sandwich structure. The specific capacitance (C_{cell} ,

F g⁻¹), energy density (E , Wh kg⁻¹) and power density (P , W kg⁻¹) of the symmetric supercapacitor cell were estimated with the equation (2), (3) and (4) as following [21] :

$$C_{cell} = \frac{I \times \Delta t}{m \times \Delta V} \quad (2)$$

$$E = \frac{C_{cell} \times \Delta V^2}{2} \quad (3)$$

$$P = \frac{E}{\Delta t} \quad (4)$$

Where, I (A) represents the current, ΔV (V) is the potential window, Δt (h) is the discharge time, and m (g) indicates the total mass of the active material on the working electrode, respectively.

3. RESULTS AND DISCUSSION

3.1. Morphology, composition and structure analysis

The morphology of SPC, DPC and HPC were investigated by SEM and TEM. Fig. S1a and S1c exhibited that SPC has a kind of aggregation structure with a coarse surface and irregular shape. The TEM images in Fig. S1b and S1d further illustrated the aggregated coarse surface of the resin after carbonization. There are some micropores formed in the carbonized resins because of the obvious decomposition at 750 °C (Fig. S3). There are a lot of pores in DPC as shown in Fig. S2a and S2b which are densely dotted in the carbonized resins and the size of these pores is about 15 nm. The high magnification TEM image (Fig. S2b) clearly showed that the carbon materials possesses obvious mesoporous structure and the pore size is further analyzed by BET. As shown in Fig. S2c and S2d, the DPC manifests rough surface and the dense interconnected mesopores can be observed clearly in Fig. S2d.

The morphology of HPC was shown in Fig. 1. As shown in Fig. 1a, 1b and 1c, it is obvious that numerous mesopores and macropores exist in HPC because of the addition of 15 nm and 100 nm SiO₂ nanospheres. The TEM images of SiO₂ nanospheres and SEM pictures of macroporous carbon materials were shown in Fig. S4. Confirmed by Fig. 1d, the surface of HPC was very rough and many macropores emerged on the surface of the HPC. The high magnification SEM images (Fig. 1e and 1f) showed that the distribution of mesoporous and macroporous was disordered. But the micropore of carbon materials was not very clear because the low resolution. The distribution of N and S in HPC was examined by EDS, and the result showed that both N and S were uniformly distributed throughout the entire aggregation (Fig. 1d and 1e, inset).

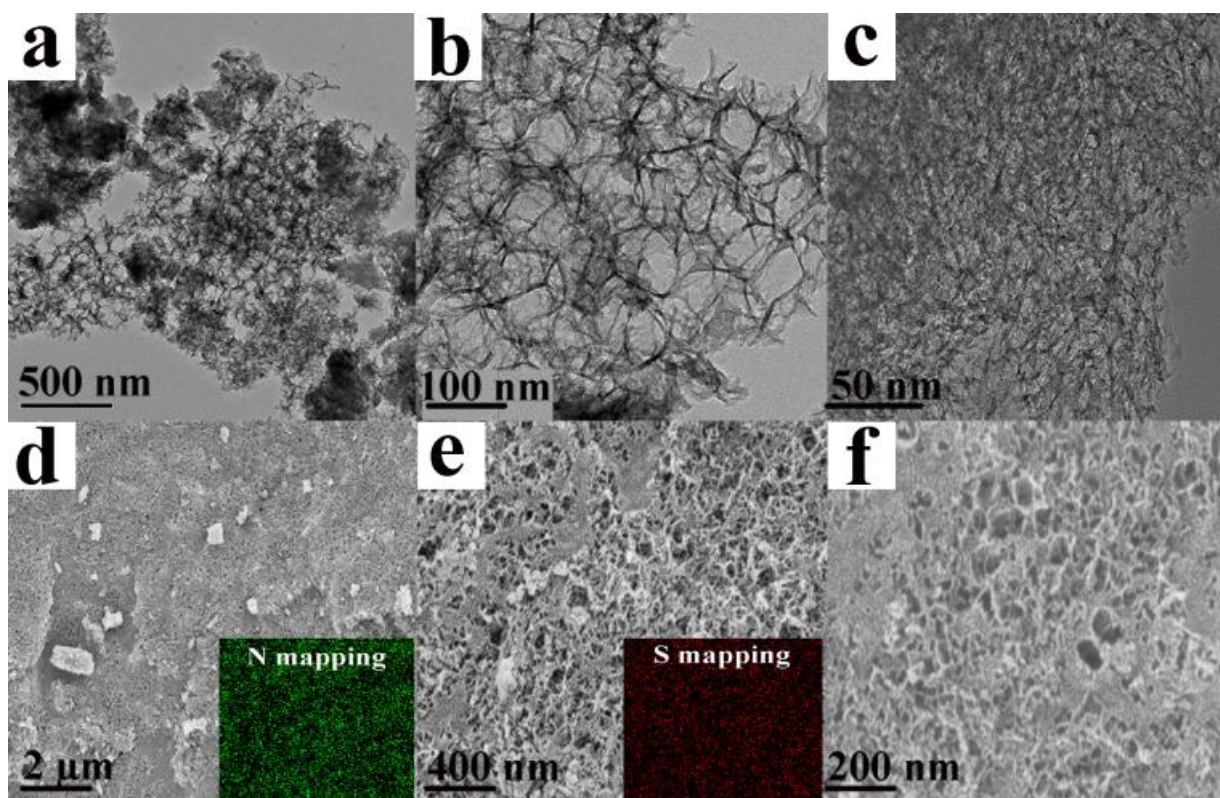


Figure 1. (a, b, c) TEM and (d, e, f) SEM images of HPC

Fig. 2a showed the FTIR spectra of SPC, DPC and HPC. The peak at 3423 cm^{-1} belongs to the -NH group, and the peaks located at 2922 cm^{-1} and 2852 cm^{-1} are ascribed to the asymmetrical and symmetrical vibration of -CH_2 respectively. The peak at 1618 cm^{-1} belongs to the vibration and deformation of -NH_2 and the band at 1384 cm^{-1} is due to the C=S stretching vibrations [36, 37]. In addition, the peak at 1114 cm^{-1} is because of the asymmetrical vibration of Si-O-Si which illustrates that there is trace amount of SiO_2 in the sample because of incomplete alkaline etching [38]. Compared with the SPC, the basic characteristic vibration absorption peaks existed in DPC and HPC which hints the chemical structure of the three samples is similar.

The XRD patterns recorded for SPC, DPC and HPC were shown in Fig. 2b. In the XRD pattern of all samples, two weak and broad characteristic diffraction peaks locate at about $2\theta=26^\circ$ and $2\theta=44.2^\circ$, which are connected with the (002) and (100) lattice planes, respectively. This result indicates that the materials are mild graphitized, which incarnates some advantages in improving the electrochemical performance and the electrical conductivity of supercapacitors at some level [39, 40]. The peak intensities of (002) and (100) for all samples were similar, illustrating that the templates and process of alkaline etching had little effect on the crystallinity of materials.

The results of Raman spectroscopy were presented in Fig. 2c, and it clearly showed that all of the samples have two similar bands at nearly 1355 cm^{-1} (D band) and 1567 cm^{-1} (G band), which are corresponding to the disordered graphite carbon (sp^3 -hybridized carbon) and graphitic carbon phase (sp^2 -hybridized carbon), respectively [41, 42]. It is found that the D/G intensity ratio ($I_D/I_G = 1.12$) in HPC higher than that of DPC ($I_D/I_G = 1.00$) and SPC ($I_D/I_G = 0.90$), because the molecular structure of polymer

resin were influenced by templates and the graphitizing degree of HPC, DPC and SPC gradually increases [43, 44].

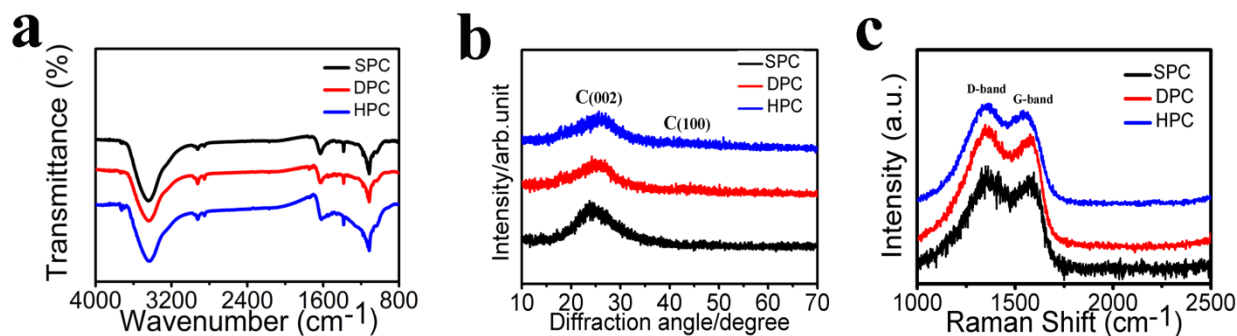


Figure 2. (a) FTIR spectra, (b) XRD spectra and (c) Raman spectra of SPC, DPC and HPC

XPS characterizations were used to prove the successful nitrogen and sulfur co-doped and detailed atomic environment of nitrogen and sulfur in HPC. As exhibited in the Fig. 3a, two small peaks corresponding to doped atoms occurred in the spectrum of HPC, indicating N and S heteroatoms were successfully introduced into the porous carbon materials. The XPS results showed that the atomic percentage of N and S was 17.56% and 0.39%, respectively. And the atomic percentage of SPC and DPC was listed in Table S1. The high-resolution N 1s spectrum exhibited four binding energy at 397.8, 399.2, 400.2 and 400.9 eV as shown in Fig. 3b, corresponding to the pyridinic-N, pyrrolic-N, and oxidized-N respectively. And the pyridinic-N and pyrrolic-N have a high binding ability with electrolyte cations and quaternary graphitic nitrogen plays an important role in improving the electronic conductivity of the materials [45, 46]. As shown in Fig. 3c, the S 2p spectrum exhibits three peaks at 163.4, 164.5 and 167.8 eV. The peaks at 163.4 eV and 164.5 eV were corresponded to S 2p_{3/2} and S 2p_{1/2} respectively [47, 48]. And the peak located at 167.8 eV was due to the oxidized sulfur [43]. The sulfur atom increased the activity of materials and facilitated the electrochemistry reaction. In addition, the polarization of sulphur is awfully notable and brings pseudocapacitances into materials [47].

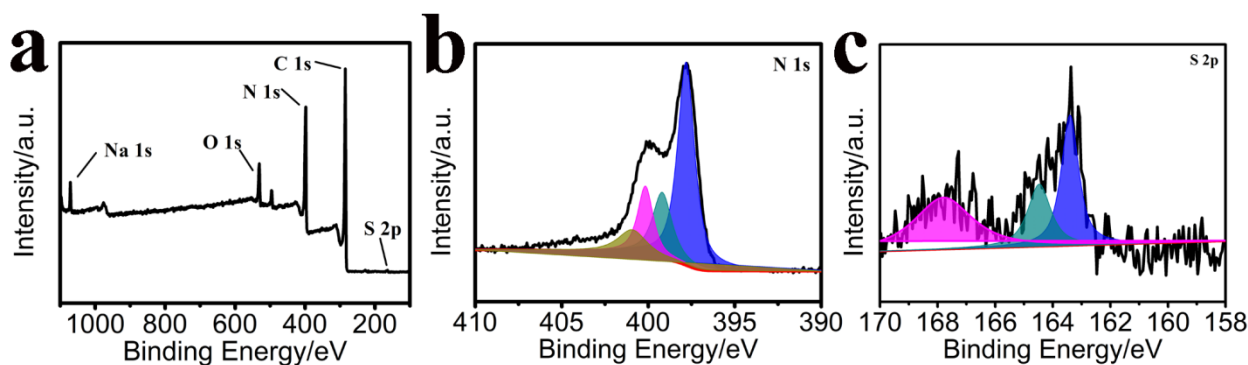


Figure 3. (a) XPS survey spectrum, (b) N 1s spectrum and (c) S 2p spectrum of HPC

Nitrogen adsorption/desorption isotherms and pore size distribution curves of SPC, DPC and HPC were presented in Fig. 4 and all samples exhibited the shape combining type-I and type-IV [49].

There were a linear increase in the low pressure region ($P/P^0 < 0.1$) and a hysteresis loop in the high pressure region ($P/P^0 > 0.4$) in N_2 adsorption of HPC. This adsorption/desorption characteristic indicates that the hierarchical pore structure exists in the prepared materials [28, 39]. And at the same time, as exhibited in Fig. 1, macropores can be clearly seen. By comparison with SPC and DPC, HPC had a highest adsorption plateau at the low relative pressure region, indicating lots of micropores come into being. In Table S2, the S_{BET} of SPC was $59.5 \text{ m}^2 \text{ g}^{-1}$, and the total pore volume and microporous volume were $0.1420 \text{ cm}^3 \text{ g}^{-1}$ and $0.0022 \text{ cm}^3 \text{ g}^{-1}$. The DPC had a much higher S_{BET} ($409.1 \text{ m}^2 \text{ g}^{-1}$) compared with SPC, besides the total pore volume and microporous volume were 0.7171 and $0.0225 \text{ cm}^3 \text{ g}^{-1}$ respectively, meaning more mesopores are formed in DPC after alkaline etching. Compared with SPC and DPC, HPC had the highest S_{BET} ($578.8 \text{ m}^2 \text{ g}^{-1}$) and total pore volume ($1.2586 \text{ cm}^3 \text{ g}^{-1}$). Micropores, mesopores and macropores can be introduced into HPC at the same time as energy storage reservoir adsorbing electrolyte ion, shortening charge transport distance and accelerating charge transfer [31].

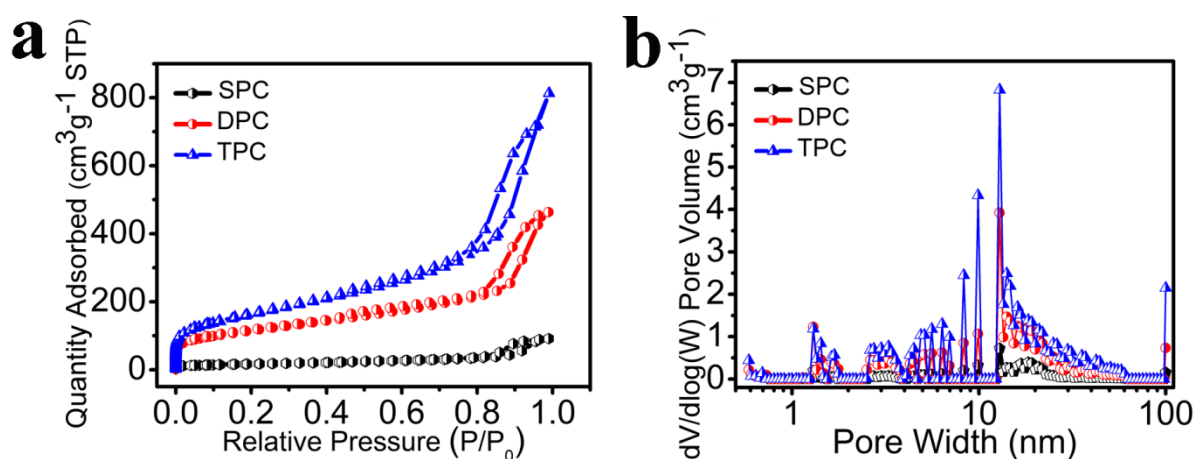


Figure 4. (a) The nitrogen adsorption/desorption isotherms and (b) pore size distribution curves of SPC, DPC and HPC.

3.2. Electrochemical performance

The electrochemical properties of all the samples were evaluated by cyclic voltammetry (CV), galvanostatic charge-discharge (GCD) and electrochemical impedance spectroscopy (EIS) measurements in three-electrode system, two-electrode system and the corresponding results were shown in Fig. 5, Fig. 6 and Fig. 7.

Fig. 5a exhibited the CV curves of the SPC, DPC and HPC electrode materials at a scan rate of 100 mV s^{-1} . It is clear that all CV curves had slightly deviation from rectangle owing to the combination of EDLC and pseudo-capacitance [50]. It is obvious that the HPC plot has the largest surrounded area compared with DPC and SPC, illustrating the best electron storage ability among the three sample.

The Fig. 5b and 5d showed the GCD curves at 1 A g^{-1} and the C_g values ranging from 1.0 to 10 A g^{-1} the SPC, DPC, and HPC electrodes. Based on Fig. 5b and 5d, the C_g of HPC was 625 F g^{-1} , much higher than that of the SPC with 135 F g^{-1} and DPC with 319 F g^{-1} . This result is consistent with that of the CV test.

EIS of all the carbon materials was achieved with the frequency range from 10^5 to 0.01 Hz in three-electrode system. As shown in Fig. 5c, HPC showed the steepest slope among all the linear curves in the low-frequency region, indicating that HPC had the lowest electrolyte ion diffusion resistance and best capacitive behavior. The equivalent series resistance (R_s) was calculated based on the real axis intercept, the charge transfer resistance (R_{ct}) was related to the diameter of the plotted semicircle in the electrode materials [51]. Calculated from Fig. 5c, the R_s of SPC, DPC and HPC were 1.25, 1.42 and 1.51 Ω , respectively. Meanwhile, R_{ct} of HPC was 0.43 Ω which is smaller than that of SPC (0.61 Ω) and DPC (1.38 Ω).

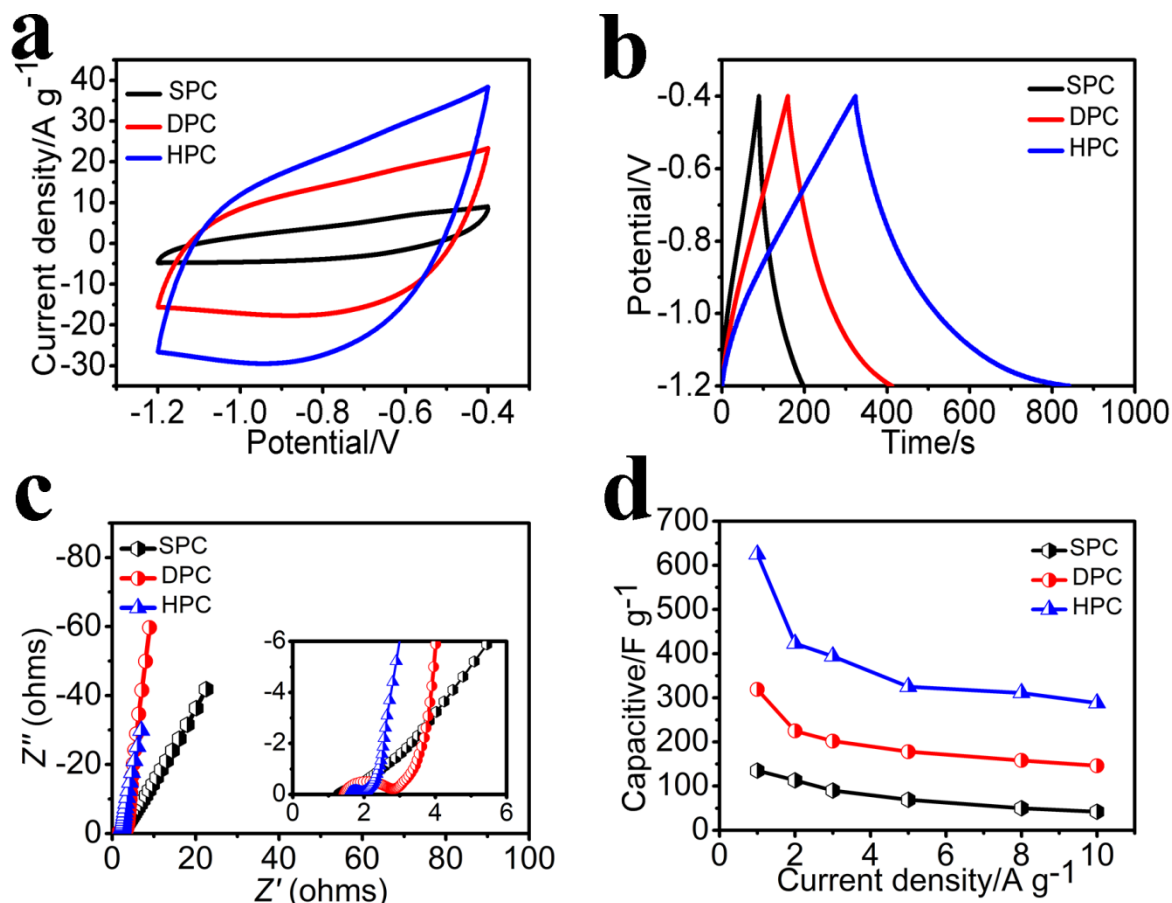


Figure 5. (a) CVs of SPC, DPC and HPC at a scan rate of $100\ mV\ s^{-1}$; (b) GCD curves of SPC, DPC and HPC at $1\ A\ g^{-1}$; (c) Nyquist plots of SPC, DPC and HPC and (d) the C_g at different current densities.

Fig. 6a exhibited the rate-dependent CV curves of HPC at different scan rates from 10 to $100\ mV\ s^{-1}$, and CV curves maintain quasi-rectangular shapes. And as shown in Fig. 6b, the C_g of HPC was $288\ F\ g^{-1}$ at a discharge current density of $10\ A\ g^{-1}$ which indicated its good rate capability of HPC. The CV and GCD curves of SPC and DPC were shown in Fig. S5. It is obvious that the surrounded area by CV curves of SPC and DPC was much smaller than that of HPC and the discharge time by GCD curves of SPC and DPC was much shorter than that of HPC, illustrating the specific capacitance and the rate capability were not very ideal and the electrochemical performances of HPC was greatly improved owing to the hierarchical pore structure and the N and S co-doping.

The cycling stability of HPC was further researched by a long-term charge-discharge cycling test at a scan rate of 10 A g^{-1} over 5000 cycles and the result shown in Fig. 6c. It revealed that the cycle stability of HPC was very outstanding and the capacitance retention was 96.08% after 5000 cycles. As shown in Fig. 6d, the Ragone plot of HPC was calculated. The high energy density of 12.5 Wh kg^{-1} at the power density of 288 W kg^{-1} was achieved, and remained as 8 Wh kg^{-1} at 7200 W kg^{-1} .

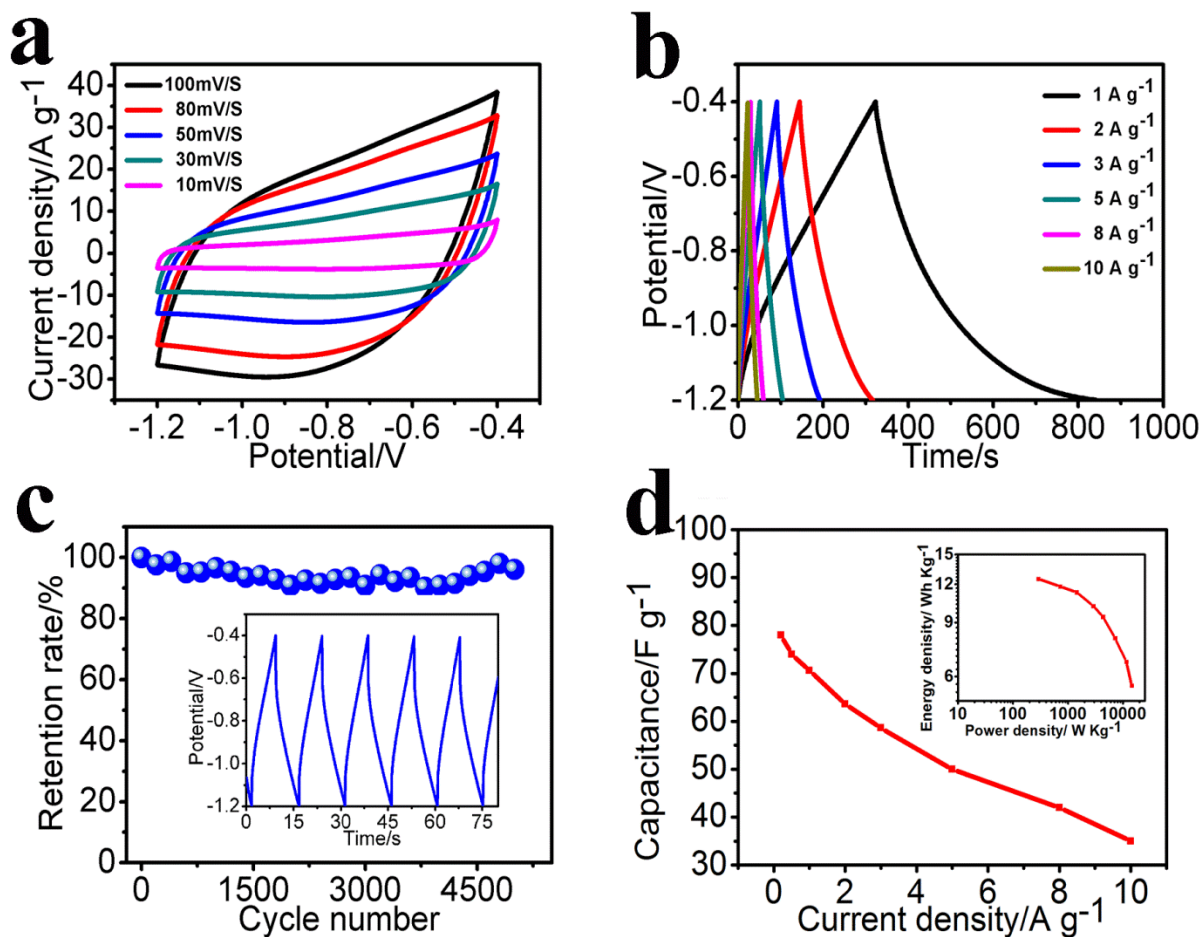


Figure 6. (a) CVs of HPC at scan rates from 10 to 100 mV s^{-1} ; (b) GCD curves of HPC at different current densities; (c) The cycling stability of HPC at a current density of 10 A g^{-1} and (d) Ragone plot of HPC

The electrochemical performances of HPC based on the symmetrical cell in 1 M LiPF_6 in EC/DEC were tested and the corresponding results were shown in Fig. 7. The fusiform CV curves in Fig. 7a represent the combination of electrical double layer capacitor and pseudocapacitance. The R_s and R_{ct} of HPC were 0.93 and 2.26Ω , respectively, as shown in Fig. 7c. The HPC shows outstanding capacitive reversibility because the GCD curves possess a wonderful symmetry as exhibited in Fig. 7b and 7d. The cell capacitance C_{cell} was 35.7 F g^{-1} at the current densities 0.2 A g^{-1} and 12.8 F g^{-1} at 10 A g^{-1} in 1 M LiPF_6 in EC/DEC electrolyte, revealing the rate capability of HPC needs to be improved [52]. E and P are calculated using the GCD data and the corresponding result of Ragone plot of HPC was exhibited at the inset of Fig. 7d. The E of HPC is 44.6 Wh kg^{-1} when the P of HPC is 300 W kg^{-1} .

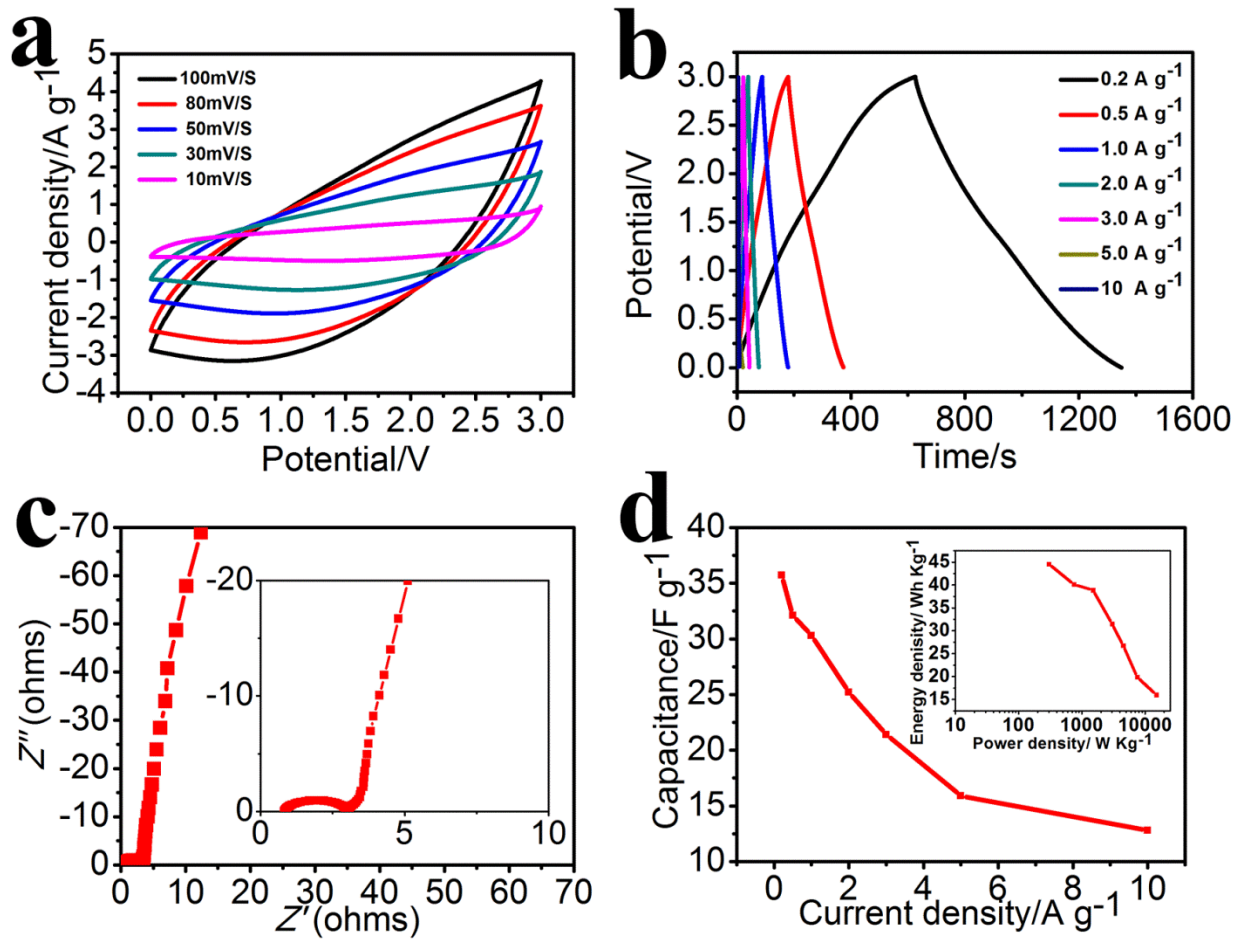


Figure 7. (a) CVs of HPC at scan rates from 10 to 100 mV s⁻¹; (b) GCD curves of HPC at different current densities; (c) Nyquist plots of HPC and (d) Ragone plot of HPC at 1 M LiPF₆ in EC/DEC electrolyte.

Table 1. The Comparison of specific capacitance and the ratio of heteroatom of similar materials

Electrode material	Electrolyte	Specific capacitance	S _{BET} (m ² g ⁻¹)	heteroatoms	Retention	Ref.
HPC	6M KOH	625 F g ⁻¹ at 1.0 A g ⁻¹	578.8	N (17.56%), S(0.39%)	96.08% after 5000 cycles	This work
PM	1M H ₂ SO ₄	278 F g ⁻¹ at 0.1 A g ⁻¹	568	N(5%), P (0)	108% after 5000 cycles	24
SNC	6M KOH	250 F g ⁻¹ at 0.2 A g ⁻¹	850	N (2.1%), S (1.3%)	-----	34
HPCs	6M KOH	283 F g ⁻¹ at 1.0 A g ⁻¹	1371	-----	95.86% after 10000 cycles	27
NPCs	1M H ₂ SO ₄	343 F g ⁻¹ at 0.5 A g ⁻¹	3381	N (2.08%)	100% after 5000 cycles	33
NSLPC	6M KOH	243.4 F g ⁻¹ at 0.1 A g ⁻¹	1689	N (8.17%), S (1.97%)	94% after 5000 cycles At 3A g ⁻¹	53
PAC	3M KOH	380 F g ⁻¹ at 1 A g ⁻¹	2760	N (1.71%), S (0.76%), P (0.57%)	96% after 10000 cycles	54
NSO-HPC	1M H ₂ SO ₄	382 F g ⁻¹ at 0.3 A g ⁻¹	---	N (7.63%), S (0.65%)	93.7% after 10000 cycles At 10A g ⁻¹	55

Table 1. shows performances of different heteroatoms doped porous carbon materials published in recent years. Apparently, the specific capacitance of HPC is the highest among the electrodes listed in Tab. 1 although its S_{BET} is not very high. Its stable cycling capability is near to the similar materials and its N content is rich after heat treatment. The simple and effective route provides a promising strategy to prepare electrode as supercapacitors.

4. CONCLUSION

To summarize, hierarchical porous carbon materials (HPC) with nitrogen and sulfur heteroatoms have been successfully prepared with different size of SiO_2 as template, followed by carbonization and further process of alkaline etching. The as-prepared HPC has large surface area, hierarchical porous structure and rich nitrogen and sulfur heteroatoms. Benefiting from these structure advantages, the specific capacitance of HPC reaches 625 F g^{-1} at 1.0 A g^{-1} with excellent rate capability (288 F g^{-1} at 10 A g^{-1}) and cycling stability at 10 A g^{-1} (96.08% after 5000 cycles) in three-electrode system using 6 M KOH as electrolyte. At the same time, the energy density of HPC was 12.5 and 44.6 Wh kg^{-1} at the power density of 288 and 300 W kg^{-1} in 6 M KOH electrolyte and 1 M LiPF_6 in EC/DEC system. So HPC can be used a promising electrode for supercapacitors with outstanding electrochemical performances.

ACKNOWLEDGMENTS

This study was supported by the first batch of Natural Science Foundation of Shandong Province (Grant No. ZR 2015BM001) and the Natural Science Foundation of Shandong Province, China (Grant No. ZR 2016EMB16). The Welch Foundation (V-0004) was acknowledged.

SUPPLEMENTARY INFORMATION

S1. TEM and SEM images of SPC

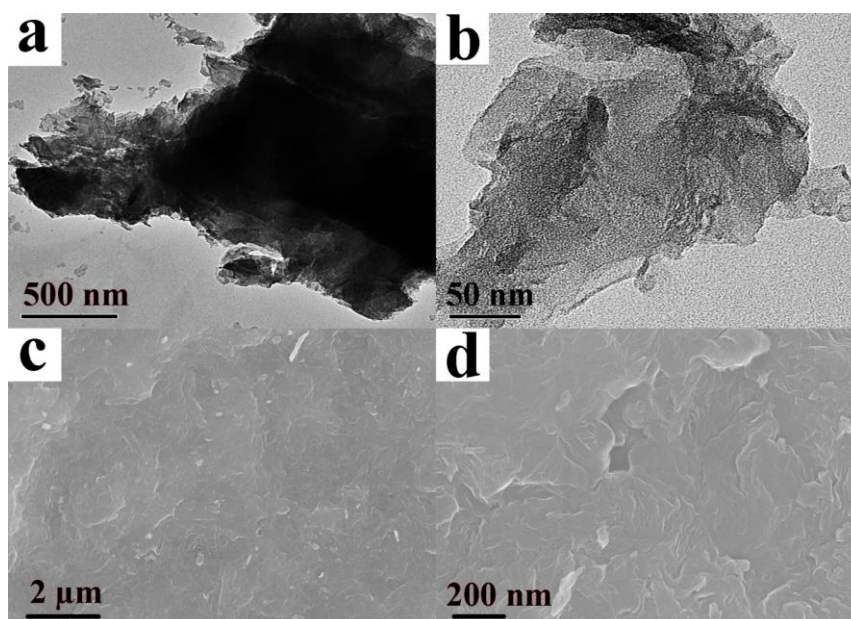


Figure S1 (a, b) TEM and (c, d) SEM images of SPC

S2. TEM and SEM images of DPC

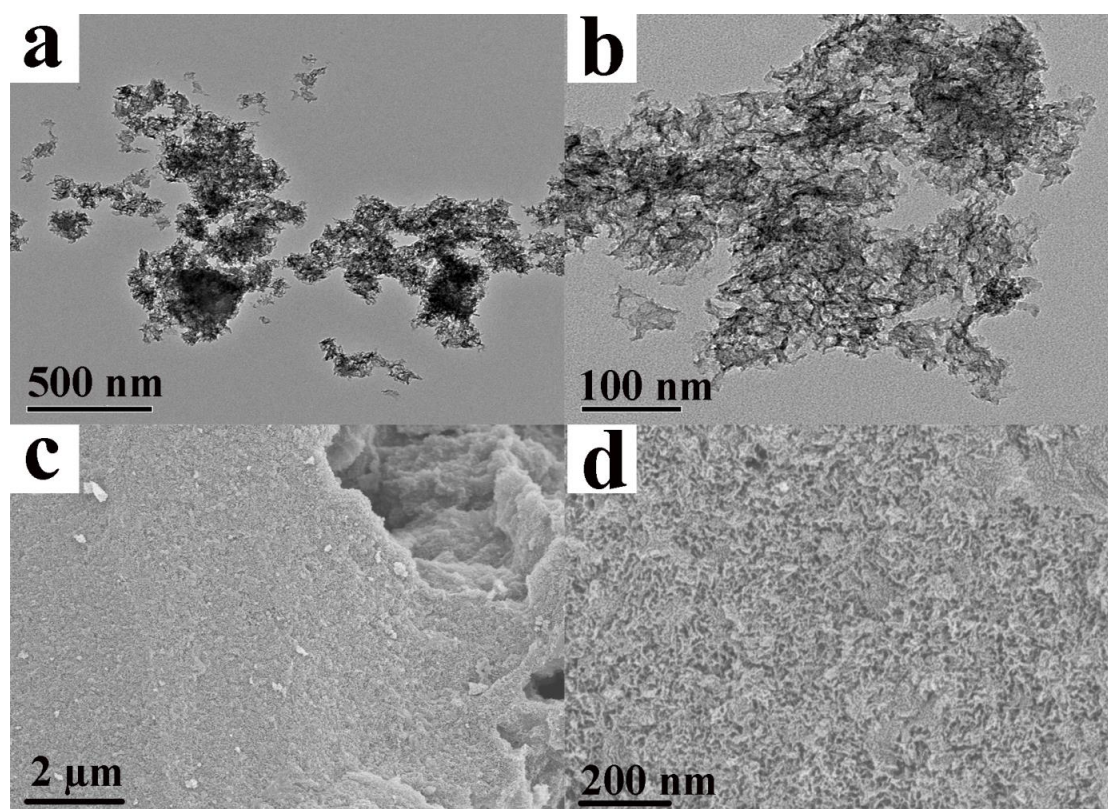


Figure S2 (a, b) TEM and (c, d) SEM images of DPC

S3. TGA curves of the SPC

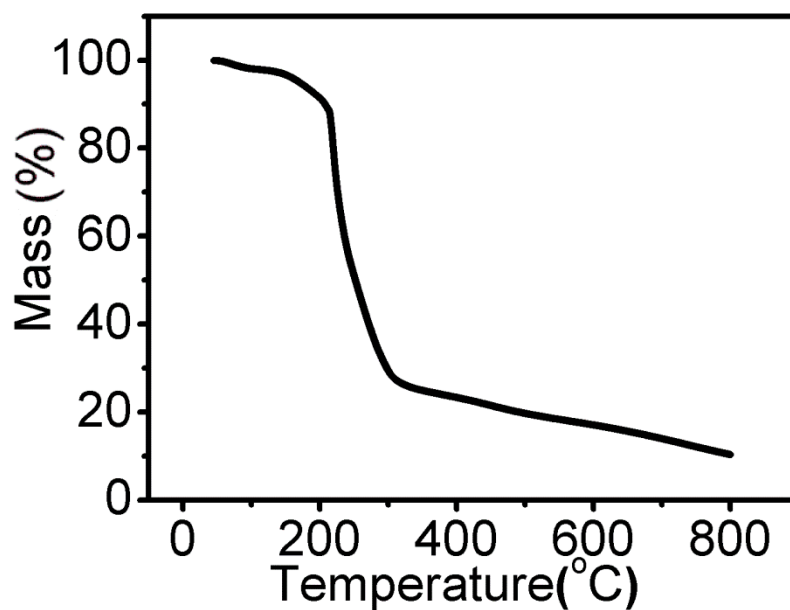


Figure S3 TGA curves of the SPC

S4. TEM images of SiO₂ nanospheres and SEM images of macroporous carbon materials

Fig. S2a and 2b exhibited that the diameter of SiO₂ nanospheres was about 100 nm, and the dispersibility was very nice. The macroporous carbon materials were prepared when used SiO₂ nanospheres as template. Fig. S2c and 2d showed the SEM of macroporous carbon materials and the morphology of macroporous carbon materials was a sort of honeycomb structure and the diameter of built hole was about 100 nm. In addition, there are bits of 30-40 nm mesoporous existed in the inside and wall of the hole.

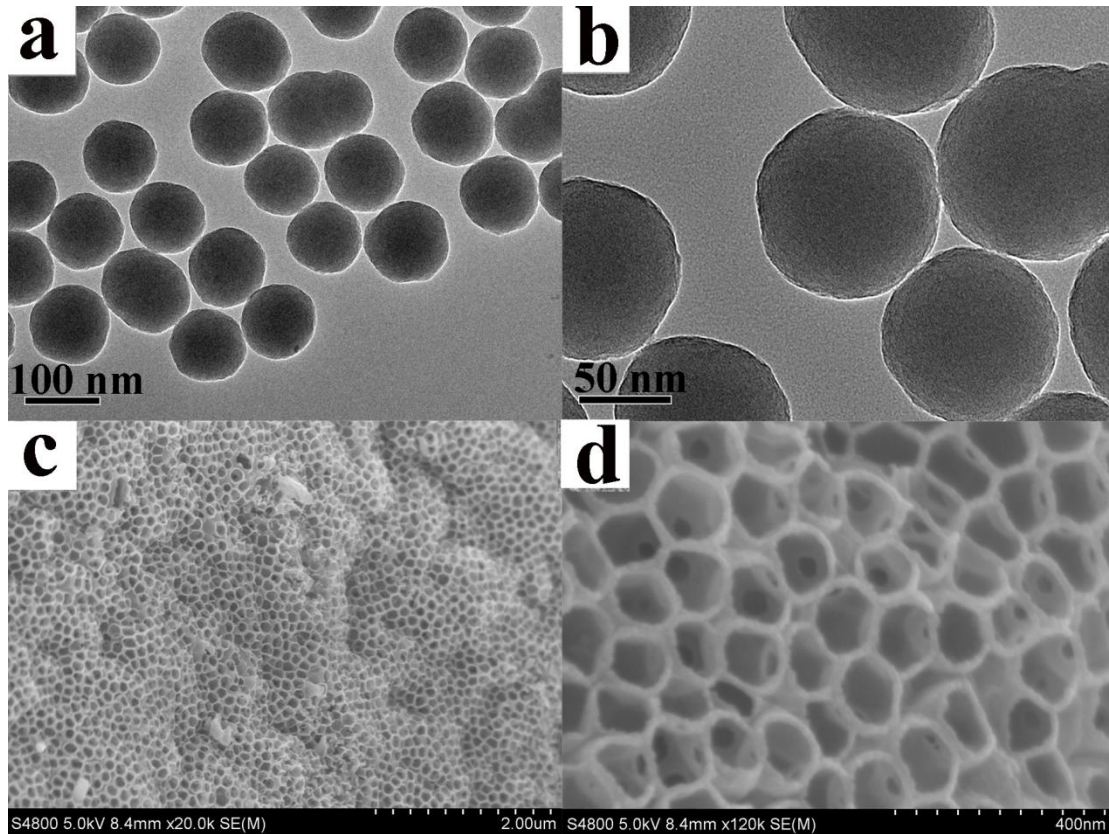


Figure S4 (a, b) TEM images of SiO₂ nanospheres and (c, d) SEM images of macroporous carbon materials

S5. XPS analysis

Sample	C (at.%)	O (at.%)	N (at.%)	S (at.%)
SPC	76.65	6.17	16.29	0.89
DPC	76.49	6.06	16.62	0.84
HPC	76.19	5.87	17.56	0.39

S6. BET analysis

sample	BET analysis				
	S_{BET} ($\text{m}^2 \text{g}^{-1}$)	V_{total} ($\text{cm}^3 \text{g}^{-1}$)	V_{micro} ($\text{cm}^3 \text{g}^{-1}$)	S_{micro} ($\text{m}^2 \text{g}^{-1}$)	$S_{\text{micro}} / S_{\text{BET}}$
SPC	59.5	0.1420	0.0022	5.1	8.6%
DPC	409.1	0.7171	0.0225	53.4	13.1%
HPC	578.8	1.2586	0.0080	21.9	3.8%

S7. Electrochemical performances of SPC and DPC

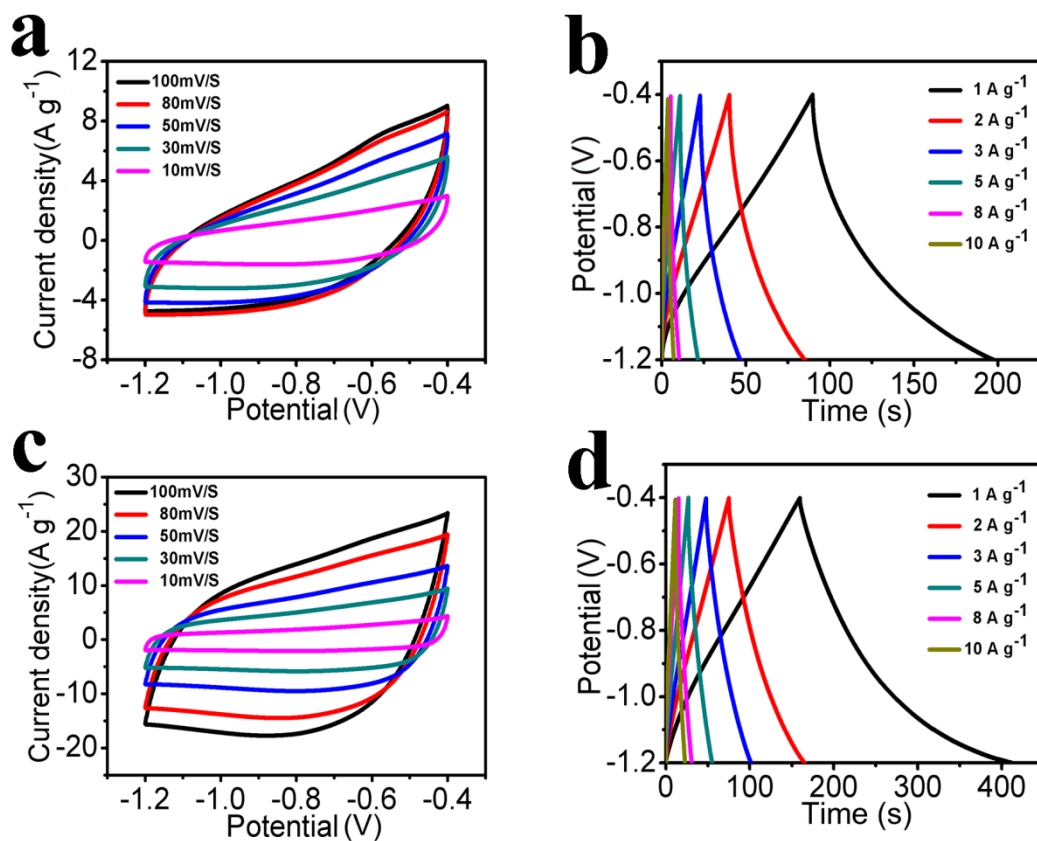


Figure S5 (a, c) CVs of SPC and DPC at scan rates from 10 to 100 mV s^{-1} ; (b, d) GCD curves of SPC and DPC at different current densities.

S8. Performance comparison of carbon symmetric SCs

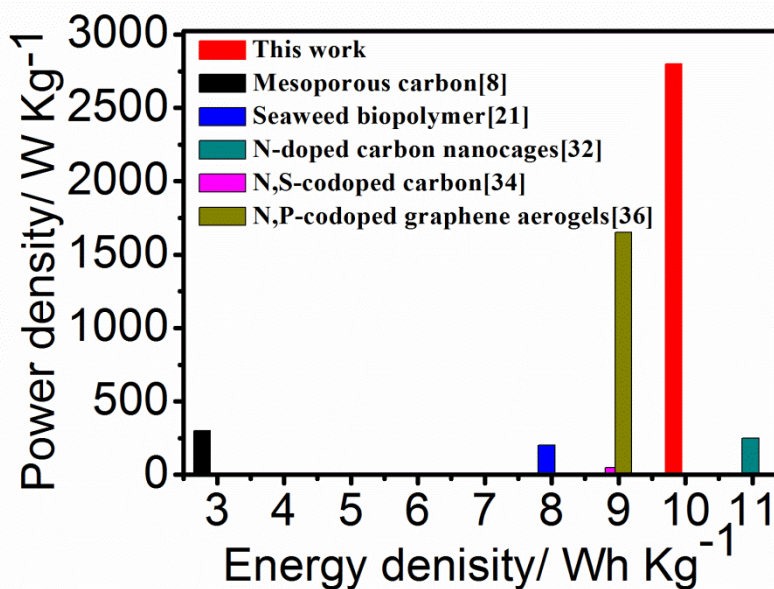


Figure S6 Performance comparison of the present symmetric cell versus previously reported carbon symmetric SCs in aqueous electrolytes.

References

1. K. Xia, Q. Gao, J. Jiang, J. Hu, *Carbon*, 46 (2008) 1718.
2. Z. S. Wu, G. Zhou, L. C. Yin, W. Ren, F. Li and H. M. Cheng, *Nano Energy*, 1 (2012) 107.
3. E. Frackowiak and F. J. C. Béguin, *Carbon*, 39 (2001) 937.
4. D. Zhu, Y. Wang, L. Gan, M. Liu, C. Ke, Y. Zhao, X. Deng and D. Sun, *Electrochim. Acta*, 158 (2015) 166.
5. R. Kotz and M. J. E. A. Carlen, *Electrochim. Acta*, 45 (2000) 2483.
6. Y. Zhao, M. Liu, X. Deng, L. Miao, P. K. Tripathi, X. Ma, D. Zhu, Z. Xu, Z. Hao and L. Gan, *Electrochim. Acta*, 153 (2015) 448.
7. L. Jiang, Q. Cheng, Y. Xia, V. Pavlinek, P. Saha and C. Li, *J. Mate. Sci.*, 49 (2014) 7489.
8. A. B. Fuertes, F. Pico and J. M. Rojo, *J. Power Sources*, 133 (2004) 329.
9. H. Li, L. Jiang, Q. Cheng, H. Ying, V. Pavlinek, P. Saha and C. Li, *Electrochim Acta*, 164 (2015) 252.
10. O. Ghodbane, J. L. Pascal, F. Favier, *Acs Appl. Mater. Interfaces*, 1 (2009) 1130.
11. Z. Yang, J. Ren, Z. Zhang, X. Chen, G. Guan, L. Qiu, Y. Zhang and H. Peng, *Chem. Rev.*, 115 (2015) 5159.
12. H. Wang and L. Pilon, *J. Power Sources*, 221 (2013) 252.
13. F. Baizeng, K. Jung Ho, K. Min-Sik, *Acc. Chem. Res.*, 46 (2013) 1397.
14. P. Simon, and Y. Gogotsi, *Acc. Chem. Res.*, 46 (2013) 1094.
15. W. Deng, Y. Zhang, L. Yang, Y. Tan, M. Ma and Q. Xie, *Rsc Adv.*, 5 (2015) 13046.
16. L. Zhi, Z. Xu, H. Wang, D. Jia, B. Zahiri, C. M. B. Holt, X. Tan, D. J. E. Mitlin, *Energy Environ. Sci.*, 7 (2014) 1708.
17. J. Wang, S. Feng, Y. Song, W. Li, W. Gao, A.A. Elzatahry, D. Aldhayan, Y. Xia, D. Zhao, *Catal. Today*, 243 (2015) 199.
18. X. Hong, K. S. Hui, Z. Zhi, K. N. Hui, L. Zhang, M. Mo and L. Min, *Electrochim. Acta*, 130 (2014) 464.
19. X. Zhao, L. Yin, Z. Tong, Z. Min, Z. Fang, C. Wang, Y. Wei, C. Gang, Z. Dong and Z. Sun, *Nano*

- Energy*, 49 (2018) 137.
20. L. Z. Li, G. Yi and X. S. J. J. o. M. C. A. Zhao, *J. Mater. Chem. A.*,1 (2013) 9395.
 21. W. Xing, C. C. Huang, S. P. Zhuo, X. Yuan, G. Q. Wang, D. Hulicova-Jurcakova, Z. F. Yan and G. Q. Lu, *Carbon*, 47 (2009) 1715.
 22. E. R. Piñero, F. Leroux, F. Béguin, *Adv. Mater.*, 18 (2010) 1877.
 23. H. J. Liu, J. Wang, C. X. Wang and Y. Y. Xia, *Adv. Energy Mater.*,1 (2011) 1101.
 24. B. You, J. Jiang and S. Fan, *ACS Appl Mater & Inter* , 6 (2014) 15302.
 25. J. Jiang, H. Chen, Z. Wang, L. Bao, Y. Qiang, S. Guan, J. Chen, *J. Colloid Interf. Sci.*, 452 (2015) 54.
 26. Y. Song, S. Hu, X. Dong, Y. Wang, C. Wang, Y. Xia, *Electrochim. Acta*, 146 (2014) 485.
 27. Y. Song, Z. Li, K. Guo and T. Shao, *Nanoscale*, 8 (2016) 15671.
 28. D. Zhu, Y. Wang, W. Lu, Z. Hong, Z. Song, L. Dong, L. Gan, M. Liu and D. Sun, *Carbon*, 111 (2017) 667.
 29. W. Shen, W. Fan, *J. Mater. Chem. A.*, 1 (2013) 999.
 30. T. Panja, D. Bhattacharjya, J.S. Yu, *J. Mater. Chem. A.*, 3 (2015) 18001.
 31. L. Zheng, Z. Wang, M. Zhang, Y. Chang, W. Gang, Y. Dong, S. Liu, Y. Wang and J. Qiu, *Adv. Funct. Mater.*, 26 (2016) 111.
 32. J. Li, K. Liu, X. Gao, B. Yao, K. Huo, Y. Cheng, X. Cheng, D. Chen, B. Wang and W. Sun, *ACS Appl. Mater. & Inter.*, 7 (2015) 24622.
 33. J. Zhao, H. Lai, Z. Lyu, Y. Jiang, K. Xie, X. Wang, Q. Wu, L. Yang, Z. Jin and Y. Ma, *Adv. Mater.*, 27 (2015) 3541.
 34. Y. Wang, X. Yan, M. Tu, J. Cheng and J. Zhang, *Mater. Lett.*,191 (2017) 178.
 35. Z. Jin, H. Shen, Z. Li, Z. Shuai, Y. Zhao, B. Xu, Y. Wang, H. Cui and S. Zhuo, *Electrochim. Acta*, 209 (2016) 557.
 36. Z. Jiawei, C. Yurong, Z. Qiwei, L. Dongzhi and Y. Juming, *Nanoscale*, 7 (2015) 17791.
 37. W. Zhong-Shuai, W. Andreas, C. Long, S. Yi, T. Andrey, F. Xinliang and M. Klaus, *Adv. Mater.*, 24 (2012) 5130.
 38. A. B. Fuertes and S. J. C. Alvarez, *Carbon* , 42 (2004) 3049.
 39. Y. Xia, Y. Zhu and Y. I. J. C. Tang, *Carbon*, 50 (2012) 5543.
 40. N. Fechler, T. P. Fellingner and M. Antonietti, *J. Mater. Chem. A*, 1 (2013) 14097.
 41. G. Xu, B. Ding, P. Nie, L. Shen, J. Wang and X. Zhang, *Chemistry*, 19 (2013) 12306.
 42. J. Liang, Y. Jiao, M. Jaroniec and S. Z. Qiao, *Angew Chem.*, 51 (2012) 11496.
 43. J.P. Paraknowitsch, J. Zhang, D. Su, A. Thomas, M. Antonietti, *Adv. Mater.*, 22 (2010) 87.
 44. P. Jens Peter, T. Arne and S. J. C. C. Johannes, *Chem. Commun.*, 47 (2011) 8283.
 45. N. Q. Tran, B. K. Kang, M. H. Woo and D. H. J. C. Yoon, *Chem. Sus. Chem.*, 9 (2016) 2261.
 46. L. Mei, Y. Zhang, L. Yang, Y. Liu and J. J. E. A. Yao, *Electrochim. Acta*, 166 (2015) 310.
 47. S. Wang, L. Gai, J. Zhou, H. Jiang, Y. Sun and H. Zhang, *J. Phys. Chem. C.*, 119 (2015) 3881.
 48. G. Sun, L. Ma, J. Ran, L. Bing, X. Shen and T. J. E. A. Hua, *Electrochim. Acta*, 194 (2016) 168.
 49. Y. Deng, Y. Xie, K. Zou, X. Ji, *J. Mater. Chem. A.*, 4 (2016) 1144.
 50. J. Liu, J. An, Y. Ma, M. Li and R. Ma, *J. Electrochem. Soc.*,159 (2012) A828.
 51. S.K. Meher, G.R. Rao, *J. Phys. Chem. C.*,115 (2011) 15646.
 52. Z. L. Li and X. S. Zhao, *Chem. Soc. Rev.*, 38 (2009) 2520.
 53. J. Li, G. Zhang, C. Fu, L. Deng, R. Sun, C.-P. Wang, *J. Power Sources*, 345 (2017) 146.
 54. M. Xu, D. Li, Y. Yan, T. Guo, H. Pang, and H. Xue, *RSC Adv.*, 7 (2017) 43780.
 55. W. Yang, W. Yang, A. Song, L. Gao, L. Su, G. Shao, *J. Power Sources*, 359 (2017) 556.